Daily monitoring algorithms to detect geostationary imager visible radiance anomalies

David R. Doelling,[a,*] Conor Haney,[b] Rajendra Bhatt,[a] Benjamin Scarino,[b] and Arun Gopalan[b]

[a]NASA Langley Research Center, Hampton, Virginia, United States
[b]Science Systems and Applications Inc., Hampton, Virginia, United States

Abstract. The NASA Clouds and the Earth's Radiant Energy System (CERES) project provides observed flux and cloud products for the climate science community. Geostationary satellite (GEO) imager measured clouds and broadband derived fluxes are incorporated in the CERES SYN1deg product to provide regional diurnal information in between Sun-synchronous Terra and Aqua CERES measurements. The recently launched GEO imagers with onboard calibration systems have active calibration teams that incrementally update the calibration in order to mitigate calibration drifts. However, short-term L1B radiance anomalies and calibration adjustment discontinuities may still exist in the record. To avoid any GEO cloud and flux artifacts in the CERES SYN1deg product, these calibration events must be addressed while scaling the GEO imagers to the Aqua-moderate resolution imaging spectroradiometer (MODIS) calibration reference. All-sky tropical ocean ray-matching (ATO-RM) and deep convective cloud invariant target (DCC-IT)-based monitoring algorithms are presented to detect calibration-driven daily anomalies in the GOES-16 Advanced Baseline Imager L1B visible (0.65 μm) radiance measurements. Sufficient daily ATO-RM sampling was obtained both by ray-matching GOES-16 with multiple MODIS and visible-infrared imaging radiometer suite imagers as well as by increasing the grid resolution. Optimized angular matching and outlier filtering were most effective in reducing the ATO-RM daily gain algorithm noise. The DCC-IT daily calibration algorithm utilized a larger domain and included more GOES-16 scan times. The DCC-IT daily gain uncertainty was reduced by normalizing the DCC regional reflectance on a regional, seasonal, and diurnal basis. The combination of ATO-RM and DCC-IT daily monitoring algorithms is shown to detect, with a high degree of confidence, daily GOES-16 L1B calibration-driven radiance anomalies >2.4%, while keeping false positives at a minimum. Remarkably, the ATO-RM and DCC-IT daily gains are mostly within 0.5%. The ATO-RM and DCC-IT daily monitoring algorithms can be easily adapted to other GEO imagers and visible channels. [DOI: 10.1117/1.JRS.16.014502]

Keywords: GOES-16; daily monitoring; ray-matching intercalibration; deep convective cloud calibration.

Paper 210401 received Jun. 25, 2021; accepted for publication Dec. 14, 2021; published online Jan. 10, 2022.

1 Introduction

The NASA Clouds and the Earth's Radiant Energy System (CERES) project monitors the Earth's energy balance and provides the climate science community with Earth reflected solar and emitted broadband flux products.[1,2] CERES instruments are flying on the Terra, Aqua, NPP, and NOAA-20 low-Earth orbit (LEO) Sun-synchronous satellites, which have a local equator crossing time of 10:30 am, 1:30 pm, 1:30 pm, and 1:30 pm, respectively. The CERES instrument measured radiances need to be converted to fluxes using angular directional models,[3] which are based on the cloud properties retrieved from the accompanying moderate resolution imaging spectroradiometer (MODIS) or visible infrared imaging radiometer suite (VIIRS) imagers.[4–6] The CERES project relies on five contiguous, concurrent geostationary satellite (GEO) imagers

*Address all correspondence to David R. Doelling, david.r.doelling@nasa.gov

to infer the regional diurnal flux signal in between CERES measurement periods.[7] Consistent MODIS, VIIRS, and GEO cloud properties and radiances are necessary to compute climate-quality fluxes across satellite platforms. For CERES Edition 4 (Ed4) SYN1deg product, the GEO imager radiances are radiometrically scaled to the Aqua-MODIS Collection 6.1 (C6.1) band 1 (0.65 μm) calibration reference by intercalibrating all-sky tropical ocean ray-matched (ATO-RM) GEO and MODIS radiances pairs.[8] In this preliminary study, the L1B calibration event detection algorithms are formulated and demonstrated for the GOES-16 Advanced Baseline Imager (ABI) 0.65-μm channel, which is the only channel used in the CERES SYN1deg Ed4 product to estimate the SW flux. The algorithms will be expanded in future to incorporate other reflective solar channels of GOES-16 ABI.

Himawari 8/9 Advanced Himawari Imager[9] and GOES-16/17 ABI[10,11] were the first GEO sensors to have onboard visible calibration systems via use of onboard solar diffusers. The optical throughput of all satellite-based visible imagers degrades over time due to the harshness of the space environment. This degradation can be estimated using Earth invariant targets, such as deep convective clouds, deserts, or polar ice, or by intercalibrating against well-calibrated sensors, e.g., Aqua-MODIS. The temporal degradation is then usually modeled using linear, polynomial, or exponential equations.[8,12] However, the new GEO imagers with onboard calibration may account for the visible channel degradation by allowing for frequent, maintenance-like updates to the visible channel calibration gain coefficients over time. Unlike the NASA MODIS and VIIRS datasets, which are reprocessed from the beginning of the record after correcting for calibration-induced anomalies, GEO calibration updates are simply made in real time and the record is not reprocessed.[13] This latter method may cause an L1B radiance discontinuity, which must be identified and accounted for before the GEO cloud and fluxes can be retrieved for the CERES SYN1deg product. The CERES imager and GEO calibration group has been tasked to design a processing system that can provide confident near-real-time identification of these GEO L1B calibration anomalies in order to thereafter mitigate their impact on the retrieved cloud properties and radiances and thereby meet processing deadlines.

1.1 *GOES-16 Calibration Events*

The GEO imager data systems have been designed for weather forecasting, where real-time data dissemination is paramount. The raw GOES-16 ABI image counts are transmitted to the ground segment, where the geolocation, calibration, and registration is applied.[14] The GOES-16 ABI L1B data are then retransmitted to the satellite for broadcast over the GOES-16 domain, allowing users with antennas to capture real-time images. The CERES project procures its GOES-16 ABI L1B images from the Man Computer Interactive Data Access System (McIDAS)[15] developed by the Space Science and Engineering Center at the University of Wisconsin-Madison, who employ their own antenna and archive systems while providing data display services.

The Global Space-based Inter-Calibration System (GSICS) is an international organization dedicated to the harmonization of Earth-observing satellite sensor measurements for climate monitoring, weather forecasting, and environmental applications that aim to incorporate best practices decided among the participating agencies.[16] GSICS has advocated for maintaining public facing calibration anomaly logs, which many agencies have complied with. For example, the NOAA Center for Satellite Applications and Research/National Environmental Satellite, Data, and Information Service (NESDIS) has set up a GOES ABI calibration event monitoring webpage.[13] Similar web pages exist for the JMA GMS/MTSAT/Himawari imagers[17] and the Meteosat SEVIRI imagers.[18] Table 1 summarizes the major GOES-16 visible channel calibration events. Three short-term calibration anomalies occurred during April 10, 2018, January 18 to 22, 2019, and April 8 and 9, 2019. The fourth, and current latest, event was a 6.2% band 2 (0.65 μm) calibration update that was implemented on April 23, 2019.

The GOES-16 event #1, #2, and #3 L1B calibration anomalies (Table 1) were not accounted for in the current CERES GEO Ed4 processing framework. By linearly regressing the GOES-16 and Aqua-MODIS coincident ATO-RM radiance pairs monthly, the Ed4 ATO-RM algorithm properly scaled the GOES-16 L1B reflectance values for the time prior to and following calibration event #4. Finding the exact timing of these events in the ATO-RM Ed4 processing algorithm requires dividing the month into multiple day segments and iteratively adjusting the

Table 1 GOES-16 ABI abbreviated events log containing the major visible calibration events adapted from the NESDIS webpage.[13]

Event #	Time begin	Time end	Description
1	04/10/2018	04/10/2018	All 6 VNIR channels experienced ~10% jumps due to the incorrect use of solar calibration coefficients
2	01/18/2019	01/22/2019	Incorrect VNIR bands gain began at 15:00 UTC on 01/18/2019 and ended at 16:00 UTC on 01/22/2019
3	04/08/2019	04/09/2019	All GOES-16 VNIR bands experienced a calibration discontinuity of 10%
4	04/23/2019	Present	New B02 LUT implemented, the GOES-16 B02 radiance is reduced by 6.2%

segment times until a sharp transition is discovered. This level of effort cannot be sustained in an operationally efficient manner. In this study, we present an ATO-RM and a deep convective cloud invariant target (DCC-IT) daily monitoring algorithm to detect these GOES-16 L1B calibration anomalies.

2 Methodology

2.1 *Data*

The GOES-16 full disk (FD) imager pixel-level (0.5 km nominal) visible band 2 (0.65 μm) counts are obtained from the McIDAS servers. Prior to April 2, 2019, GOES-16 scanned a FD every 15 min (scan mode 3), and after April 2, 2019, an FD is scanned every 10 min (scan mode 6).[19] The operational GOES-16 subsatellite location is 75.2° W. The Terra-MODIS and Aqua-MODIS C6.1 band 1 (0.65 μm) L1B (1-km nominal) products are utilized. The NPP-VIIRS NASA Land Science Investigator-Led Processing System (SIPS) Collection 1 L1B and NOAA20-VIIRS SIPS L1B Collection 2 (375-m nominal) I1 (0.65 μm) band pixels are employed. The VIIRS I1 band was selected over the M5 band because the spectral response of the former most closely resembles GOES-16 band 2. For this study, all imagers are subsampled at a 2-km resolution.

2.2 *Monthly-ATO-RM*

The CERES Ed4 GEO monthly ATO-RM calibration algorithm provides the framework to construct the ATO-RM daily monitoring algorithm and is briefly described here.[8] The Ed4 calibration algorithm provides the scaling factors to convert the GEO channel visible counts to a radiance that is scaled to the Aqua-MODIS C6.1 calibration reference by monthly pair-regression of MODIS and GEO coincident, angle-matched radiance pairs over ocean. The individual monthly scaling factors, or gains, are then fit with a polynomial regression to track the gains over time. The GOES-16 tropical ocean domain is bound by ±15° in latitude and 110° W to 55° W, where the domain has been shifted to the west of the subsatellite (75° W) point in order to increase the ocean coverage. All MODIS overpasses that intersect the domain are identified and matched with the closest GOES-16 FD scan. Both the MODIS and GOES-16-pixel radiances are aggregated into a 0.5° latitude by longitude grid. The MODIS and GOES-16 grid locations coincident within 15 min and where the view zenith angle, relative azimuth angle, and scattering angle are matched within 15 deg are paired, except in regions of glint. To avoid complex scene conditions, a spatial homogeneity threshold of 0.7 is applied, which is defined as the standard deviation of the samples in the grid cell divided by the sample mean.

The Ed4 monthly ATO-RM algorithm further constrains the angle matching by applying graduated angle matching (GAM).[20] For the darkest and the second darkest quartile of MODIS radiances, both the viewing and azimuthal angles are matched within 5 deg and 10 deg, respectively. GAM takes advantage of the fact that brighter, thick-cloud radiances are more Lambertian

than the darker radiances of thin clouds and clear sky conditions. The averaging of pixel radiances into a 0.5-deg grid results in a greater frequency of darker than brighter radiance regions over tropical ocean domains. The greater frequency of darker radiance allows for stricter angle matching of darker anisotropic regions. The less sampled but more Lambertian brighter regions need only loose angle matching. If the same angular restrictions were applied over the entire dynamic range, the sampling of the brighter radiance pairs would be limited, which in turns limits the dynamic range and decreases the confidence of the resulting linear regression. The MODIS radiances are adjusted to the GOES-16 solar zenith angle (SZA) and spectral response by normalizing the cosine SZA and applying a spectral band adjustment factor (SBAF) using the following equation:

$$\mathrm{Rad}_{\mathrm{MODIS}} * [\cos(\mathrm{SZA}_{G16})/\cos(\mathrm{SZA}_{\mathrm{MODIS}})] * \mathrm{SBAF}_{G16/\mathrm{MODIS}} = \mathrm{gain} * (\mathrm{CNT}_{G16} - \mathrm{CNT}^{0}_{G16}), \tag{1}$$

where CNT_{G16} represents the McIDAS 12-bit scaled radiance count for GOES-16 band 2 from the McIDAS L1B files, and CNT^{0}_{G16} is the scaled space count or offset count for zero radiance. The value of CNT^{0}_{G16} is set to 128 for GOES-16 band 2. The GOES-16 count and MODIS radiance ($\mathrm{Rad}_{\mathrm{MODIS}}$) pairs are linearly regressed monthly and the regression is forced to pass through CNT^{0}_{G16}. In this paper, the term force fit is used to refer to a linear regression through a known offset. The SBAF is based on Scanning Imaging Absorption Spectrometer for Atmospheric Chartography (SCIAMACHY) hyperspectral radiances convolved with the GOES-16 and MODIS spectral response functions over all-sky tropical ocean scenes obtained from the NASA-CERES-SCIAMACHY-based-SBAF web tool.[21–23] Linear regression through the known space count CNT^{0}_{G16} is found to more accurately predict the GOES-16 band 2 gain compared to solving for both the gain and offset.[24] A linear or second-order polynomial regression is applied to the individual monthly force fit gains to track the degradation over time.[25] The calibration coefficients are updated on a bimonthly basis for the concurrent GEOs used in the CERES record.[26]

2.3 *Daily-ATO-RM*

The daily ATO-RM algorithm greatly increases the number of coincident angle-matched radiance pairs available by: (1) combining the Aqua-MODIS/GOES-16, Terra-MODIS/GOES-16, NPP-VIIRS/GOES-16, and NOAA20-VIIRS/GOES-16 datasets; (2) using a 0.25-deg grid rather than the operational 0.5-deg grid; and (3) matching each LEO image in time with the three closest GOES-16 10 or 15 min FD scans. All Sec. 2.2 matching criteria are applied to the daily ATO-RM radiance pairs.

Although CERES currently uses Aqua-MODIS C6.1 as the GEO calibration reference, the CERES GEO monthly ATO-RM algorithm also intercalibrates Terra-MODIS, NPP-VIIRS, and NOAA20-VIIRS with GOES-16 as backups in the event of an Aqua-MODIS failure. The framework is already in place to incorporate these LEO imagers into the ATO-RM daily monitoring algorithm. The resulting GOES-16 monthly ATO-RM calibration coefficients can be used to place the LEO imagers on the same radiometric scale. The LEO imager radiances ($\mathrm{Rad}_{\mathrm{imager}}$) are converted to pseudo-GOES-16 digital counts (CNT^{P}_{G16}) by solving for CNT_{G16} in Eq. (1):

$$\mathrm{CNT}^{P}_{G16} = \mathrm{Rad}_{\mathrm{imager}} * (1.0/\mathrm{gain}) * [\cos(\mathrm{SZA}_{G16})/\cos(\mathrm{SZA}_{\mathrm{imager}})] * \mathrm{SBAF}_{G16/\mathrm{imager}} + \mathrm{CNT}^{0}_{G16}. \tag{2}$$

This allows the regressed imager pseudo- and observed GOES-16 count (CNT) pairs to have a gain of unity with an x-offset through the prescribed space CNT. Although each MODIS and VIIRS sensor is independently calibrated using onboard calibration systems, the imager relative calibration differences are removed using Eq. (2), and thus intercalibrating the imager sensors directly with each other is not required. In order to compute Eq. (2) CNT^{P}_{G16} for each of the LEO imagers, the gain in Eq. (1) is computed first. This is accomplished by computing the force fit gain from the LEO/GOES-16 ATO-RM pairs on a monthly basis.

In order to capture the GOES-16 L1B calibration anomalies over the record, the LEO imager radiances must be stable. This is accomplished by relying on DCC as invariant targets (see Secs. 2.4 and 3.5). The LEO imager DCC response is used to identify any short-term calibration drifts in the LEO imager records. No significant drifts were identified in Terra- and Aqua-MODIS L1B C6.1 calibration during 2018 to 2020. However, the NPP-VIIRS C1 L1B I1 reflectance DCC timeseries shows a positive trend of ~0.6% between 2012 and 2018, and a radiometric adjustment of ~0.6% during April 2018, when a calibration look up table (LUT) update was implemented in the C1 product in the forward processing mode (VCST private communication). The monthly DCC response timeseries for NPP-VIIRS C1 L1B I1 band is shown in Fig. 1(a) with red circles. After the April 2018 LUT change, the NPP-VIIRS I1 DCC response was found to be stable and consistent with that of 2012. For this study, these temporal drifts in the NPP-VIIRS C1 calibration were removed by deriving monthly drift correction factors based on the DCC timeseries. The monthly correction factors adjust the entire NPP-VIIRS record to the radiometric scale at the beginning of the record (2012). The blue squares in Fig. 1(a) show the NPP-VIIRS I1 band DCC monthly response derived after stabilizing the VIIRS C1 L1B record. The standard deviation of the monthly DCC timeseries is reduced by ~40% after correcting for the temporal trend and calibration discontinuity in the VIIRS C1 L1B data. Similarly, the NOAA20-VIIRS monthly DCC reflectance revealed a gradual downward trend of ~0.7% for the 3-year record beginning in January 2018. The NOAA20-VIIRS I1 radiances were scaled in a similar manner by utilizing the inverse of the DCC trend to stabilize the record. Figures 1(b) and 1(c) show the monthly LEO/GOES-16 gains and their associated temporal linear trends before and after the short-term drift corrections applied to the two VIIRS I1 radiances. After the drift corrections, the LEO/GOES-16 ATO-RM trends are more consistent and range between 0.36%/year to 0.44%/year, which reveal the actual temporal radiometric drift in the ABI calibration. The Terra-MODIS, Aqua-MODIS, NPP-VIIRS, and NOAA20-VIIRS single gains of 0.1496, 0.1522, 0.1514, and 0.1437, respectively, were applied in Eq. (2). The January 15, 2018 gains were computed from the linear trend in Fig. 1(c), thus enabling a gain of unity at the beginning of the GOES-16 record. This will allow the individual LEO/GOES-16 ATO-RM radiance pairs to be combined in order to reveal the GOES-16 L1B calibration anomalies (see Ref. 27 section 2.3 and Ref. 28 for a comprehensive review of placing the individual imagers on the same radiometric scale with respect to GOES-16).[27]

The daily force fit gains are demonstrated for April 2, 9, and 26, 2019 in Fig. 2. April 2019 contains both a calibration anomaly [see Table 1 event #3 and Fig 2(b)] and an update [see Table 1 event #4 and Fig 2(c)], and both are easily identifiable. The daily trend (temporal) standard error (DTSE) of the daily force fit gains between April 1 and 22 (excluding days 8 and 9) is 0.73% [Fig 2(d)]. This would suggest that any daily gain departures greater than three times the

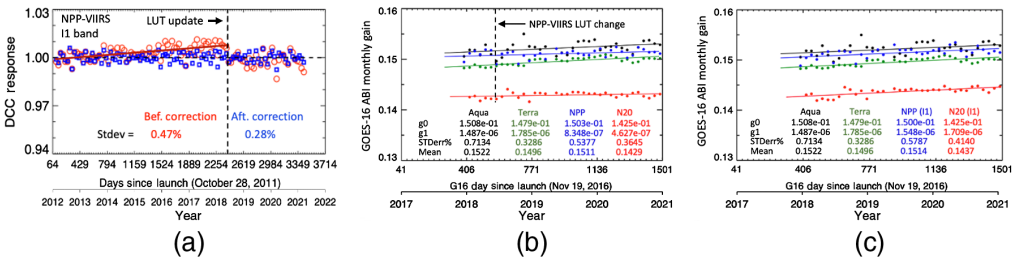

Fig. 1 (a) The NPP-VIIRS I1 band DCC response timeseries before and after drift correction. Note that the pre-LUT update DCC response is more stable and consistent with the post-LUT update record. The CERES Ed4 0.65 μm Aqua-MODIS/GOES-16 (black dots), Terra-MODIS/GOES-16 (green dots), NPP-VIIRS/GOES-16 (blue dots), and NOAA20-VIIRS/GOES16 (red dots) monthly ATO-RM force fit gains (12-bit digital counts) from Eq. (1) and associated temporal linear trend lines (b) before and (c) after drift corrections are applied to NPP and N20 VIIRS I1 band. *g*0, *g*1, STDerr%, and mean are the linear regression offset, slope (day^{-1}), standard error (%), and mean of the monthly gains, respectively. Note that before drift corrections, that the NPP and NOAA20-based GOES-16 trends were 0.20 and 0.12% year^{-1}, respectively, whereas after drift corrections the resulting GOES-16 trends were 0.37 and 0.43% year^{-1}, respectively, and were very similar to the Aqua and Terra-based GOES-16 trends of 0.36 and 0.44% year^{-1}.

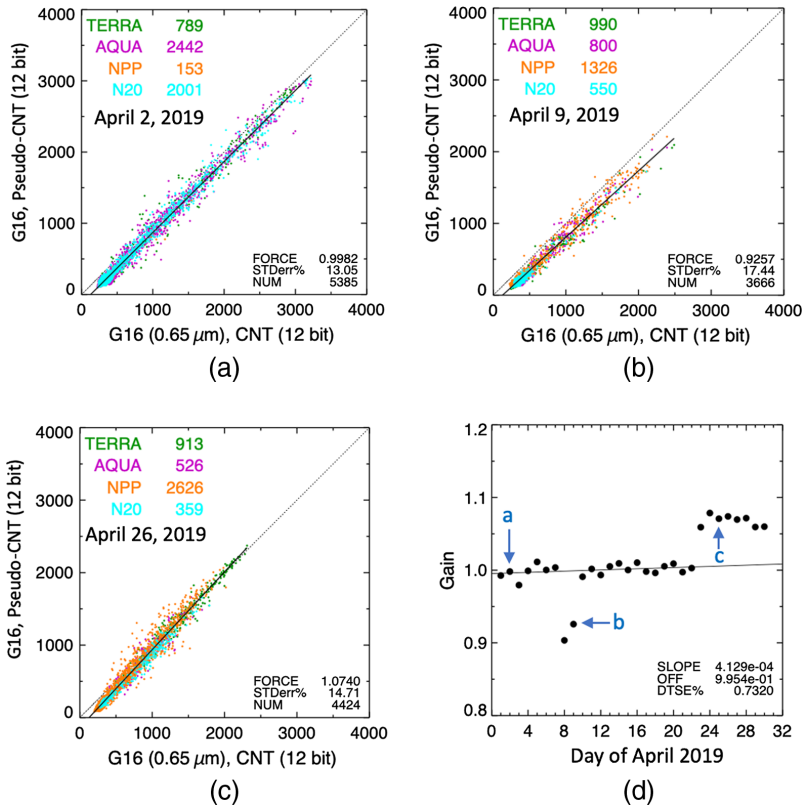

Fig. 2 April 2 (a), 9 (b), and 26 (c), 2019 daily-ATO-RM GOES-16 count and imager pseudo-count pairs. The number of imager pairs per imager is given in the upper left corner. The force fit (FORCE) gain through the GOES-16 space count of 128 counts, the linear regression standard error in % (STDerr%), and the number of radiance pairs (NUM) are shown in the lower right corner. (d) The April 2019 ATO-RM daily force fit normalized gains. The temporal linear regression slope (SLOPE), the offset (OFF), and standard error or daily trend standard error in % (DTSE%) are located in the lower right corner. The statistics are valid from 1 to 22 April and exclude the 8th and 9th. The plot also identifies the daily gains associated with (a)–(c).

DTSE (>2.5%) can be considered as a possible calibration event. Additional thresholds are examined analyzed in Sec. 3.1 in hopes of reducing the DTSE in order to detect even smaller calibration events.

2.4 *Daily-DCC-IT*

The DCC-IT daily monitoring algorithm is based on the CERES GEO monthly DCC-IT calibration algorithm and is briefly described here.[28,29] DCC are stable Earth targets when collectively analyzed for visible wavelengths because they are located near the top of the troposphere above most of the atmospheric water vapor. Tropical DCC are bright (high signal-to-noise), near-Lambertian targets. A pixel is classified as DCC if the 11-μm IR channel brightness temperature (BT) is <205 K, if the viewing and SZAs are <40 deg to ensure observation of the more Lambertian part of the angular extent, and the eight surrounding pixels have a BT and visible standard deviation or homogeneity threshold of <1 K and 3%, respectively. Both ocean and land regions are included. The GEO domain is bound by $\pm 20°$ both in longitude and latitude from the GEO subsatellite location. The Hu bidirectional reflectance distribution function is applied to the DCC identified pixel CNT in order to account for small anisotropic effects.[30] The collective pixel level GOES-16 band-2 CNTs are compiled into monthly probability density functions (PDF), and the PDF mode is tracked over time to determine the sensor degradation.

The aim of this study is to identify large daily gain shifts and having sufficient DCC sampling for all days over the record is essential. In order to increase the frequency of DCC samples, to

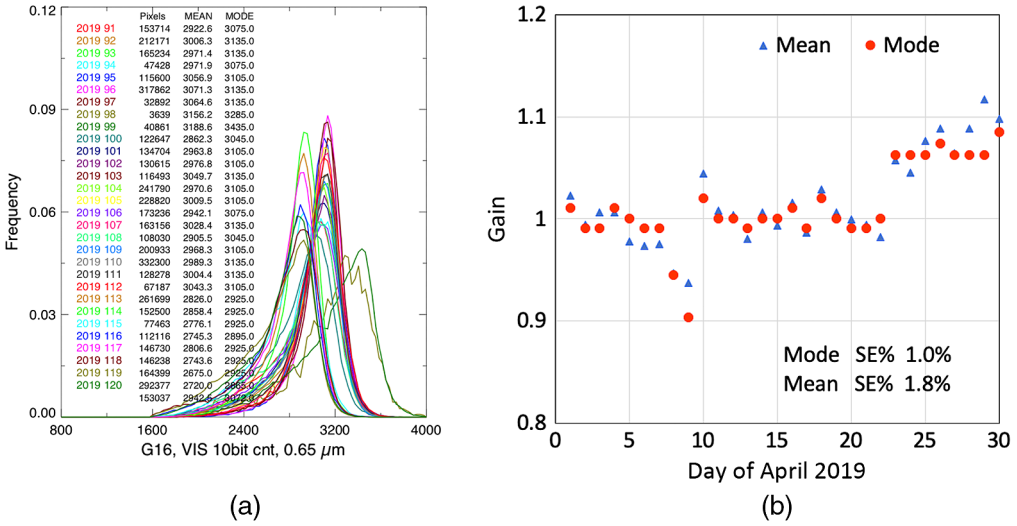

Fig. 3 (a) The April 2019 daily PDFs for GOES-16 band 2 (0.65 μm). The plot text contains the daily DCC-IT pixel frequency, PDF mean, and PDF mode in 12-bit digital counts. (b) The DCC-IT PDF daily mode and mean gains normalized to 1 to 22 April, except for 8 and 9 April. Compare Fig. 3(b) with Fig. 2(d).

thereby obtain sufficient sampling to construct robust daily PDFs, the BT threshold is increased to 210 K for daily DCC analysis. Note that the frequency of DCC pixels increases exponentially with the BT threshold.[31] The visible homogeneity threshold is also increased from 3% to 5% in order to further enhance sampling. The spatial domain is expanded, as is the number of FD scans utilized. Three spatial domains are used, all of which extend ±20° latitudinal: (1) 85° W to 45° W for the 14:00, 14:30 and 15:00 GMT FD scans, (2) 95° W to 55° W for the 15:30, 16:00, 16:30, 17:00, 17:30, 18:00 and 18:30 GMT FD scans, and (3) 105°W to 65° W for the 19:00, 19:30, and 20:00 GMT FD scans. The spatial domains migrate from east to west during the day in order to center the domain where the SZA is <40 deg.

The April 2019 daily PDFs are shown in Fig. 3(a). There appears to be sufficient daily sampling to generate consistent daily PDF shapes, where most days have over 100k identified DCC pixels. Three sets of PDFs are observed: the time-period before (April 1 to 22) and after (April 23 to 30) the calibration adjustment, as well as the April 8 and 9 calibration event (Table 1, event #3). Figure 3(a) shows that April 8, 2019 has only 3639 DCC pixels, and the corresponding PDF looks spiky but is clearly shifted right. The reduced sample size on April 8 and 9, 2019 could be due to any striping in the images (as suggested on the GOES-16 calibration event log page) that would filter out more DCC pixels during the spatial homogeneity test. The daily PDF mean and mode statistics are plotted in Fig. 3(b). The mode is clearly less noisy than the mean and is therefore the preferred PDF statistic used for DCC-IT daily monitoring. The PDF mode increment of 0.5% was selected, which balances the calibration gain discretization and PDF smoothness. The PDF mode is not impacted by the left-skewed features of the distribution, which are more than likely anvil or cloud edge pixels rather than convective core pixels. The nominal DCC-IT DTSE is 1.0%. Further algorithm refinements are applied in Sec. 3.4.

3 Results

3.1 *ATO-RM Algorithm Threshold Sensitivity Study*

To further refine the daily monitoring criteria to reduce the DTSE, each criterion is systematically analyzed by varying the threshold value while holding the remaining criterion constant. This required greatly expanding the spatial domain (115° W and 35° W and within ±30° in latitude) to increase sampling. The resulting successful refinements will be applied to the ATO-RM daily monitoring dataset in Sec. 3.2. Satellite sensor intercalibration requires eight-dimensional

matching and includes time, latitude, longitude, vertical (parallax), wavelength, as well as solar, viewing, and azimuthal angle matching.[32]

The daily GOES-16/LEO imager ray-matching pair thresholds are based on the following factors: (1) time matching difference, (2) number of GOES-16 FD scans matched to a LEO imager overpass, (3) angular matching thresholds, (4) spatial homogeneity threshold, (5) outlier filter, and (6) grid resolution. To determine the impact of a given factor, the threshold for that factor is varied while the remaining factors are kept at the baseline thresholds. The statistics are shown in Table 2. The GAM($\deg_{0<CNT<500}$, $\deg_{500<CNT<1000}$, $\deg_{CNT>1000}$) viewing and azimuthal angle restrictions in degrees are shown by the GOES-16 CNT range or quartile (see Sec. 2.2). The spatial homogeneity threshold is the grid cell GOES-16-pixel CNT standard deviation divided by the mean. The outlier filter removes ATO-RM pairs that exceed three times the linear regression standard error. Table 2 is arranged by parameter with the most restrictive threshold on the top row and least restrictive on the bottom row for a given thresholding factor. Double solid lines separate the thresholding factors. The force fit and principal components (PC) fit DTSEs are given as force fit DTSE and PC fit DTSE, respectively. The force fit uses the observed space CNT and solves only for the slope, whereas the PC fit solves for both the offset and slope simultaneously by minimizing the perpendicular or orthogonal distance to the linear regression. The mean daily fit STDerr reveals the average of the daily linear regression standard errors [Fig. 2(a) STDerr% statistic] and is based on the average of April 1 to 22 (except for April 8 and 9). The mean daily number [Fig. 2(a) NUM statistic] of ATO-RM pairs is also provided as mean daily NUM.

Clearly, the number of mean daily ATO-RM pairs is reduced as the matching thresholds become more restrictive. Due to daily sampling fluctuations, the day with the least samples essentially determines the degree of the thresholding limit that can be applied. Owing to

Table 2 The daily GOES-16/imager ATO-RM pair threshold sensitivity results (see text for details). The force fit DTSE optimized thresholds are highlighted in bold text.

Parameter	Threshold	Force fit DTSE%	PC fit DTSE%	Mean daily fit STDerr%	Mean daily NUM
Δtime (min)	5	0.39	0.77	4.3	624
	10	**0.31**	**0.42**	**5.2**	**1182**
	15	0.34	0.53	5.9	1533
# FD matched	1	0.37	0.56	4.3	621
	3	**0.31**	**0.42**	**5.2**	**1182**
GAM	1.25, 2.5, 5.0	0.43	0.72	5.0	423
	2.5, 5, 7.5	**0.31**	**0.42**	**5.2**	**1182**
	5, 10, 15	0.39	0.56	5.7	4129
	15, 15, 15	0.41	0.52	7.5	11870
Spatial σ	<0.35	0.36	0.46	3.5	491
	0.7	0.34	0.41	4.8	957
	<∞	**0.31**	**0.42**	**5.2**	**1182**
Outlier filter	**With**	**0.31**	**0.42**	**5.2**	**1182**
	Without	0.35	0.51	6.7	1240
Grid resolution	0.75 deg	0.35	0.61	2.5	132
	0.50 deg	0.36	0.50	3.3	303
	0.25 deg	**0.31**	**0.42**	**5.2**	**1182**

ATO-RM pair distribution along the radiance dynamic range, which is skewed toward the darker pairs, the matching thresholds will start to limit the bright part of the dynamic range. The bright cloudy pixels are generally less spatially homogeneous then their clear-sky counterparts. The bright cloudy pixels are also advecting, whereas clear-sky pixels are less impacted by time matching. The larger the grid resolution is, the greater the probability of averaging dark and bright pixels is, which in turn reduces the dynamic range. At some point, the sparseness of the sampling may introduce noise into the computation of the daily gains. This implies that the reduction of the mean daily fit STDerr does not guarantee a lower DTSE. The optimal time matching threshold is 10 min to obtain the smallest DTSE. The application of a spatial homogeneity filter does not reduce the DTSE. The highest grid resolution has the lowest DTSE because high resolution allows for greater sampling of bright ATO-RM pairs over the month. Increasing the number of GOES-16 FD/imager matches reduces the DTSE, suggesting that oversampling does not introduce bias. However, the additional FD scan matches have a greater time separation and therefore the mean daily fit STDerr increased. The outlier filter is very efficient in reducing mean daily fit STDerr and the DTSE without significantly reducing the number of ATO-RM pairs.

Restricting the angular matching thresholds rapidly limits the geographic locations of the ATO-RM pairs.[20,28,33] Essentially, reducing the angular matching by half will reduce the angle matching spatial domain by half. Effective angular matching will capture the tropical bright clouds that are not evenly spread out over the tropics but follow the Sun over the year. Constraining the quartile angular thresholds to GAM (2.5, 5, 7.5) is the most effective method for reducing the DTSE. However, stricter angular matching severely limits the spatial sampling and adversely impacts the DTSE. If there were a large population of strict angular-matched ATO-RM pairs, then the other factors in Table 2 may successfully reduce the DTSE.

The force fit DTSE is smaller than the PC fit DTSE. Precise angle matching for dark scenes, which are very anisotropic, are required for linear regressions that solve for both the slope and offset. The force fit linear regression takes advantage of the predetermined space CNT offset and only needs to resolve the gain. The most effective daily monitoring approach is (1) increasing the number of ray-matched pairs, (2) determining the optimal angular matching criteria, (3) applying an outlier filter and optimal time matching threshold, and (4) utilizing the force fit linear regression.

3.2 *ATO-RM Daily Monitoring*

Section 2.3 ATO-RM daily monitoring algorithm is optimized using the ATO-RM algorithm threshold sensitivity study results in Sec. 3.1. First, Table 2 GAM thresholds were tested and the smallest DTSE was achieved by applying the GAM (5, 10, 15) threshold. Utilizing the more restrictive GAM (2.5, 5, 7.5) increased the DTSE by 0.4%, and 9 days had fewer than 2 ATO-RM pairs. The time matching was left at 15 min to ensure sufficient daily sampling. The application of the spatial homogeneity threshold of 0.7 did not seem to impact the daily sampling frequency. The outlier filter was also included in the optimized dataset. The ATO-RM daily force fit gains over the 3-year record are shown in Fig. 4(a). In order to bridge the GOES-16 April 23, 2019 calibration adjustment event (see Table 1 event #4), the CNT^P was decreased by a factor of 6.2% after the event, as advised by the NOAA website. This factor was verified by comparing the post- and pre-30-day mean daily gain, which was found to be 6.02% and well within the uncertainty of the method. If the factor was unavailable on the NOAA website, this would be a reasonable forward processing approach.

Figure 4(b) shows the 6.2% factor applied after April 23, 2019. To determine anomalous daily calibration events, the DTSE, which is based on the linear trend of the daily gains over the 3-year record, is computed first. Then for each day in the record, the previous 30-day daily gain running mean is computed and plotted [Fig. 4(b) red line]. After which Fig. 4(b) two blue dotted lines, which represents ±2.7% or 3xDTSE from the running mean gain (solid red line), is plotted. Figure 4(c) shows the optimized daily gains. The optimized thresholds reduced the DTSE from 0.90% to 0.75% and the blue dotted lines were trimmed to within 2.25%. One day out of daily gain record of 1095 days had insufficient sampling utilizing the optimized thresholds. Any daily gain that exceeded the ±3xDTSE threshold is cross-checked with Table 1 events.

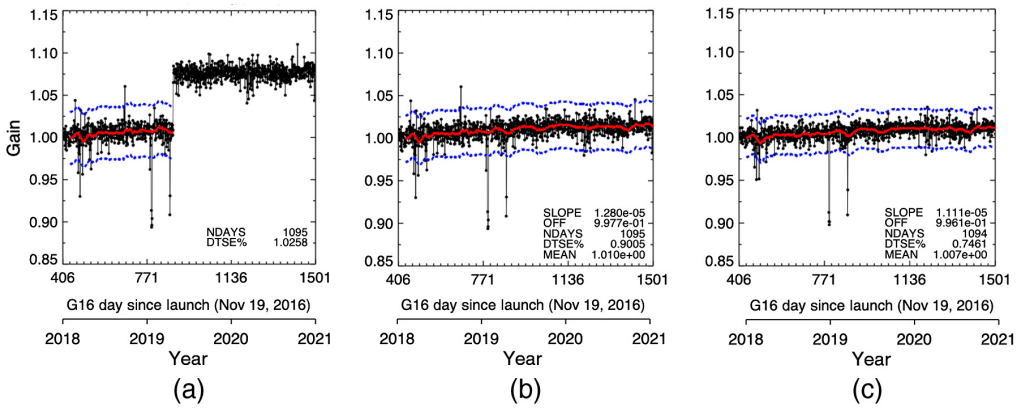

Fig. 4 (a) The 2018 to 2020 GOES-16 ATO-RM daily monitoring gains. The solid red and dotted blue lines represent the previous 30-day daily gain running mean and ±3xDTSE threshold from the running mean gain, respectively. The DTSE was based on the daily gains from January 1, 2018, until April 22, 2019 and exclude the first two calibration events listed in Table 1. (b) Same as (a) except for dividing by a factor of 1.062 to all daily gains after the April 23, 2019 and utilizing the whole record to compute the DTSE. (c) Same as (b) except for applying GAM (5, 10, and 15) and the outlier filter. The SLOPE, OFF, DTSE% are the least squares linear regression slope (day 1), offset, and standard error of the daily gains, respectively. NDAYS is the number of daily gains with sufficient sampling (1095 indicates all days sampled over the record) and the MEAN is the daily gain average over the record.

All the events in Table 1 were captured except for event #1 from April 10, 2018, when the GOES-16 band-2 calibration experienced a 10% jump. To understand why this large calibration shift was not detected by ATO-RM, the daily scatter plot for that day was examined in more detail and is discussed in Sec. 3.5. There were a few daily gains mostly in the early record that exceeded the ±3xDTSE threshold and were not associated with a known calibration event in Table 1. The number of daily gains exceeding the ±3xDTSE threshold was reduced after applying the more optimized thresholds [compare Fig. 4(b) with Fig. 4(c)]. It was noted that these noisy daily gains were associated with sparse sampling. However, most of the days with sparse sampling had robust linear regressions. A better strategy to identify calibration events would require that both ATO-RM and DCC-IT daily gains exceed their respective ±3xDTSE threshold.

3.3 *ATO-RM Monthly Trending*

Although this section does not directly pertain to the daily monitoring algorithm, it describes how the daily multi-LEO/GEO ATO-RM pair can more accurately quantify the GEO L1B temporal calibration drift. For this section, the ATO-RM algorithm incorporated GAM (5, 10, 15), a spatial homogeneity threshold of 0.7, and glint avoidance to the coincident within 15-min 0.5° gridded ray-matched pairs (see Sec. 2.2). The ATO-RM monthly optimized algorithm included the outlier filter and matching of the three closest GOES-16 FD scans per imager overpass that were within coincident within 10 min.

Figure 5(a) reveals the radiometrically scaled individual imager as well as the combined imager optimized ATO-RM monthly gains. The optimized individual imager-based monthly trend standard error (MTSE) was reduced between 8% (NOAA20) and 30% (NPP) when compared against Fig. 1(c) MTSEs. The multi-imager dataset had the lowest MTSE of 0.20%. The GOES-16 band-2 3-year degradation of 1.1% [Fig. 5(a) multi-imager] is very close to the optimized ATO-RM daily gain 3-year degradation of 1.2% [Fig. 4(c)]. The multi-imager dataset benefits from the increased monthly sampling provided by combining all imagers ATO-RM pairs, and there appears to be no negative impact by including individual imagers with larger MTSEs. The GOES-16 band-2 gain seems to stabilize after April 23, 2019, following the calibration adjustment (Table 1, event #4) and is more than likely due to the improved on-orbit performance of GOES-16. Compare Fig. 5(a) GOES-16 multi-imager monthly ATO-RM gain linear trend of 0.36% year^{-1} to Fig. 5(b) trend of 0.08% year^{-1}.

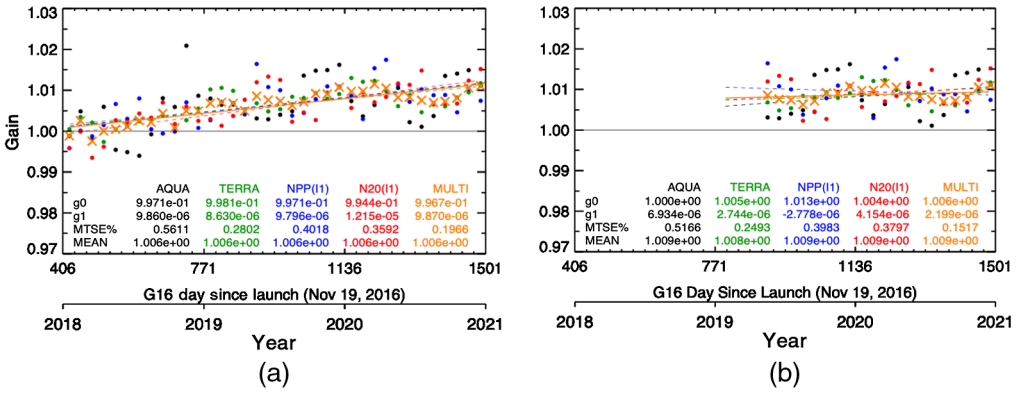

Fig. 5 GOES-16 radiometrically scaled (Eq. 2) optimized ATO-RM monthly individual imager and the multi-imager dataset (MULTI) force fit gains for the record beginning on (a) January 1, 2018, and (b) April 23, 2019. Temporal linear regression statistics are defined in Fig. 1. Note the GOES-16 temporal stability before and after April 23, 2019.

The improved sampling of the multi-imager dataset should more accurately predict the on-orbit GOES-16 space CNT than those based on the individual imagers. The GOES-16 imager looks at deep-space with every scan in order to reset the offset. Under perfect ray-matching conditions, the PC fit, which solves for both the offset and slope simultaneously should predict the predetermined CNT of 128. The Terra, Aqua, NPP, NOAA20, and multi-imager PC fit offset was 131.2, 125.3, 127.5, 126.4, and 128.1 CNTS, respectively. The multi-imager PC fit offset was within 0.1% of the true GOES-16 space CNT, whereas the individual imager PC fit offsets were between 0.4% (NPP) and 2.5% (Terra) of the GOES-16 predetermined space CNT.

3.4 *DCC-IT Daily Monitoring*

The DCC-identified pixels in Sec. 2.4 are further refined to improve the stability of the DCC response. The brightest DCC reflectance is obtained by observing the peak of the convection when the core approaches the tropopause and prior to dissipation when anvils begin to mature. This stage of the DCC lifecycle is optimal for calibration. For visible wavelengths, the DCC reflectance can vary regionally, seasonally, and diurnally.[34–37] The DCC reflectance differs over ocean and land. Over land, the convection life cycle is diurnally systematic and usually peaks in the afternoon and is also affected by terrain. Seasonally, the convective regions follow the Sun. The interannual variation of the DCC response is much smaller than the seasonal response. The PDF mode reflectance was computed for each 10° latitude by longitude grid location as a function of month (Fig. 6) and GMT time (Fig. 7) between May 2018 and April 2019. The early DCC-IT samples (January to April 2018) were not considered because they are noisier compared to the rest of the record. Three GMT time intervals were used to compute DCC reflectance diurnally: 14:00 to 16:00 GMT, 16:00 to 18:00 GMT, and 18:00 to 20:00 GMT (Fig. 7). The DCC mode reflectance is very consistent regionally, seasonally, and diurnally, except for winter

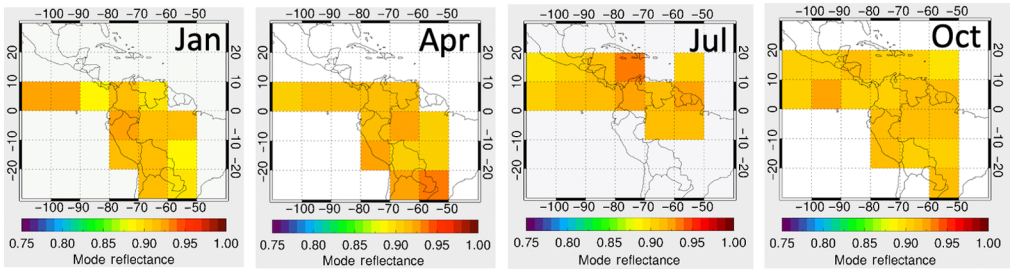

Fig. 6 10-deg gridded regional GOES-16 band 2 (0.65 μm) DCC mode reflectances for January 2019, April 2019, July 2018, and October 2018.

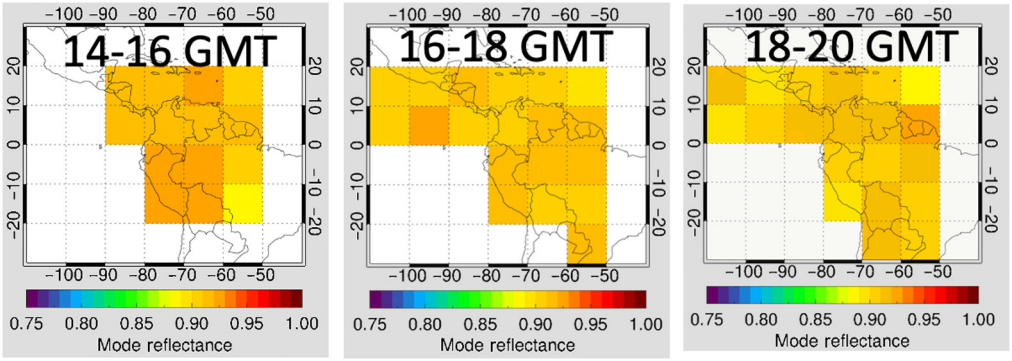

Fig. 7 10-deg gridded regional GOES-16 band 2 (0.65 μm) DCC mode reflectances as a function of GMT interval during September 2018.

months when the reflectance is slightly lower. Clearly, the DCC spatial extent does vary seasonally and diurnally. The DCC mode reflectances were compiled in an LUT as function of month, 10 deg regions, and three GMT time increments.

Figure 8(a) shows the DCC-IT daily gains without removing the April 23, 2019 gain adjustment (Table 1 event #4). Figure 8(b) removes the gain adjustment by dividing the daily gains by a factor of 1.062. Similar to Fig. 4(b), Fig. 8(b) shows the previous 30-day running mean (solid red line). The DTSE is based on the daily gain linear trend over the 3-year record. Figure 8(b) also shows the $\pm$3xDTSE threshold from the 30-day running mean (dotted blue line). Figure 8(c) shows the optimized DCC-IT daily gains that have the seasonal and diurnal LUTs applied. The application of the LUT mitigates the small seasonal variability over the record. Five days during the record had insufficient sampling to compute a robust DCC-IT gain. The DCC-IT daily monitoring algorithm can confidently identify any GOES-16 L1B anomalies $> \pm$ 2.7% or 3xDTSE of 0.90%. All Table 1 calibration events are identified by DCC-IT except for event #1. Similar to the ATO-RM daily gains, there were a few daily gains that exceeded the $\pm$3xDTSE threshold not associated with calibration events. As suggested in Sec. 3.2, DCC-IT false positive identified events are eliminated by requiring both ATO-RM and DCC-IT to identify the same daily calibration event.

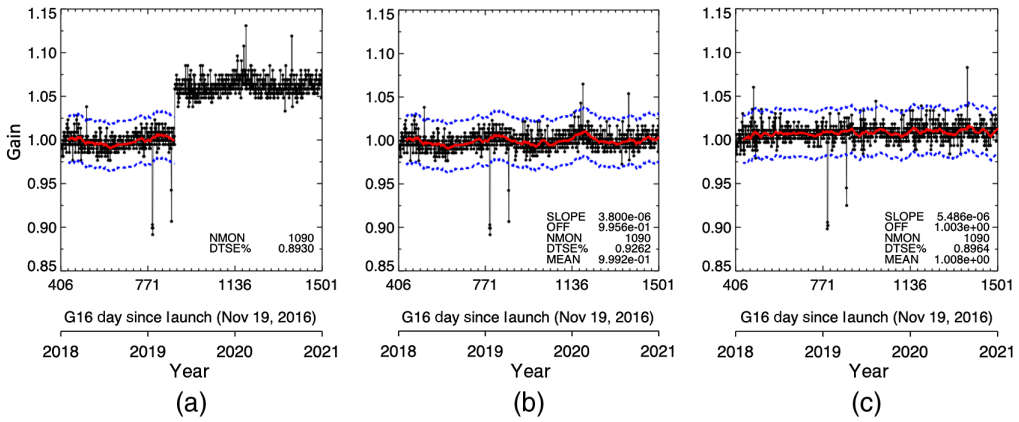

Fig. 8 (a) The 2018 to 2020 GOES-16 DCC-IT daily normalized DCC gains. The solid red and dotted blue lines represents the previous 30-day daily gain running mean and the $\pm$3xDTSE threshold from the running mean gain, respectively. The DTSE was based on the daily gains from January 1, 2018 until April 22, 2019, and excluded the first two calibration events listed in Table 1. (b) Same as (a) except for dividing by a factor of 1.062 to all daily gains after the April 23, 2019 and utilizing the whole record to compute the DTSE. (c) Same as (b) except with the LUT table applied. See Fig. 4 for a description of the lower right statistics. Note the mitigation of the seasonal variation in (c) when compared with (b).

3.5 *Real-Time Implementation*

Now that the ATO-RM and DCC-IT daily gain algorithms have been established, the forward processing or near real-time implementation procedure must be formulated. The CERES forward processing requires the GEO data to be processed within 2 months of real time. This allows the 30-day running mean to be implemented. The 30-day daily gain running mean could be impacted by large daily gain fluctuations that arise from insufficient sampling or algorithm noise that could mask subtle calibration events. A simple scaler Kalman filter, which should dampen the larger daily gain fluctuations, is utilized in forward processing. The initial predicted gain was set to 1.0, and the process noise and measurement noise coefficients were set at 0.0001 and 0.1, respectively, in order to resemble the 30-day running mean as shown in Fig. 9(d). Increasing the weights can dampen the daily gain noise as well as the daily outliers, whereas decreasing the weights might hide the daily outlier within the daily gain noise. The ATO-RM and DCC-IT 3-year DTSE, which assumes a linear calibration drift, will not be known in near real-time implementation. The forward processing daily gain noise is estimated using the root-mean-square-error (RMSE) based on the observed ATO-RM or DCC-IT daily gain and the Kalman filter predicted daily gain (KFPDG) difference. The initial RMSE is computed from the first 30 days of the record, after which the record RMSE is updated daily. Outside of a short-term radiance anomaly, the record RMSE is a combination of the ATO-RM or DCC-IT methodology daily natural variability dependent on sampling and cloud conditions as well as the embedded daily sensor noise. Any ATO-RM or DCC-IT daily gain that exceeds $\pm$3xRMSE from the KFPDG is identified as a possible calibration event. Confirmed calibration event daily gains are not used to compute or update the RMSE. There could still be daily gain outliers due to mostly methodology noise. To eliminate methodology noise outliers, both ATO-RM and DCC-IT methods must identify the same day to be considered an outlier. The larger the daily gain outlier magnitude is, the greater the confidence for detecting the L1b radiance anomalies is. Also there could be calibration events that are within the 3x the RMSE, which cannot be confidently identified with this strategy. In addition, if an event only lasts for a fraction of the day and occurred outside the sampling time of the two methods, it might not be detectable. Any undetected radiance anomalies will impair the hourly GEO cloud retrievals and the corresponding surface fluxes in the CERES SYN1deg product. However, the impact of those undetected radiance anomalies will be less severe compared to that caused by larger magnitude calibration events. Therefore, the two automated algorithms presented in this paper are believed to detect major daily changes in the GEO L1b radiance calibration with minimal human intervention and assist improving the regional day-to-day GEO surface flux variability.

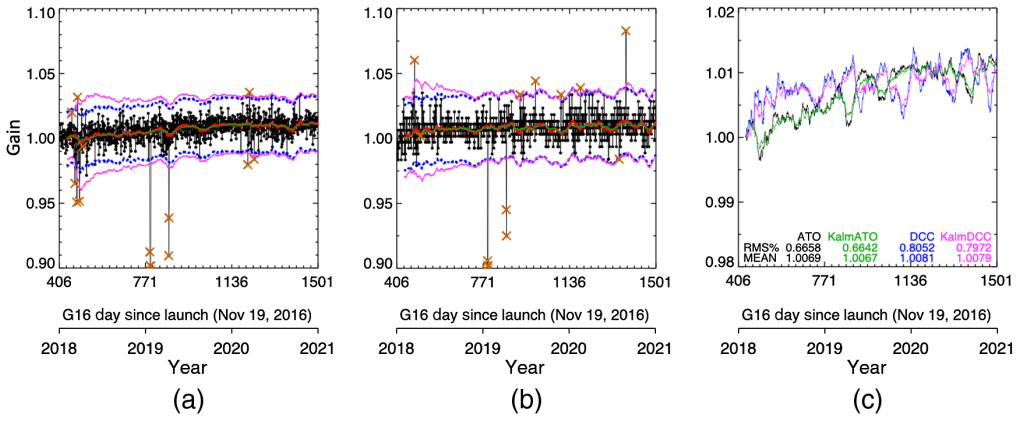

Fig. 9 The GOES-16 (a) ATO-RM and (b) DCC-IT daily normalized gains. The solid red and dotted blue lines are the same as Fig. 4c for (a) and Fig. 8c for (b). The KFDPG (solid green line) and the $\pm$3xRMSE threshold from the KFPDG (solid magenta line) are also shown. Suspected calibration event days are shown as a dark orange x. (c) The Kalm-ATO-RM (green line) and Kalm-DCC-IT (magenta line) KFPDG, which are the same as the solid green lines in (a) and (b), respectively, are compared. Note the similarity of the KFPDG lines with the ATO-RM (black line) and DCC-IT (blue line) 30-day running mean.

Figures 9(a) and 9(b) show the ATO-RM and DCC-IT daily gain forward processing strategy, respectively. The solid red and dotted blue lines are the same shown in Figs. 4(c) and 8(c), whereas the KFPDG and the ±3xRMSE threshold from the KFPDG are plotted as the solid green and solid magenta lines. The suspected daily calibration events are shown as a dark orange x. Both DCC-IT and ATO-RM individually identified possible calibration event days, but they were eliminated by requiring both the algorithms to detect the same calibration event. If both ATO-RM and DCC-IT show the same daily calibration anomaly, the anomaly is cross-checked with the calibration events log page. Together the ATO-RM and DCC-IT identified Table 1 calibration events except for event #1 that occurred on April 10, 2018, when all reflective solar channels experienced nearly a 10% jump in calibration due to incorrect solar calibration coefficients incorporated in the L1B processing. The official GOES-16 calibration log page has recorded this anomaly as a single-day event, but it does not specify the time of occurrence and duration of this anomaly. The daily DCC-IT results suggest that this calibration shift occurred only for a few hours of the day. Figure 10(a) shows the GOES-16 band-2 daily DCC PDF for April 10, 2018. The PDF for this day is bimodal and exhibits two peaks. The left peak represents the mode of the DCC pixel radiances with correct calibration applied, whereas the right peak corresponds to the DCC pixels that are impaired by the 10% calibration jump. Multiple executions of the daily DCC-IT algorithm along with a parametric sweep allowing the time of DCC pixel acquisitions to vary with a step size of 1 h revealed that the April 10, 2018 calibration anomaly only affected the GOES-16 images prior to ~19:00 GMT. The DCC-IT daily monitoring algorithm, on automatic run, computes the daily PDF mode based on the dominant peak of the PDF, which, on April 10, 2018, corresponds to the unimpaired DCC pixels acquired after 19:00 GMT. As such, event #1, which lasted for only a fraction of the day, was not successfully captured by DCC-IT. Likewise, the daily ATO-RM GOES-16 and four LEO imager pseudo-count pairs for the same day also show bimodal distribution as depicted in Fig. 10(b). The GOES-16 gridded counts that are ray-matched with Terra-MODIS (AM orbit), represented by the green circles, are shifted toward right due to the 10% jump in GOES-16 calibration, whereas the GOES-16 counts ray-matched with the remaining three LEO imagers in PM orbits tend to result in a typical regression slope as most of the GOES-16 matches for these imagers are acquired after 19:00 GMT. Because the Terra-MODIS matches constitute only a small fraction of the total daily RM samples, the combined ATO-RM regression slope is biased more toward the RM pairs from the afternoon orbiter imagers, thereby unable to detect the short-lasted event #1.

Figure 9(c) shows the KFPDG for ATO-RM and DCC-IT. The ATO-RM daily gain record was normalized to January 15, 2018 as described in Sec. 2.3. The DCC-IT record was normalized to unity using the daily DCC-IT responses during January 2018. Both the ATO-RM and DCC-IT KFPDG track each other after April 2019. During the first 6 months, the DCC-IT KFPDG reveals a sharp increase in the GOES-16 channel-2 gain and then a small gradual increase in the gain, whereas the ATO-RM KF-PDG shows a steady increase in the GOES-16 record prior to April 2019 and then a small gradual increase in the gain similar to the GOES-16

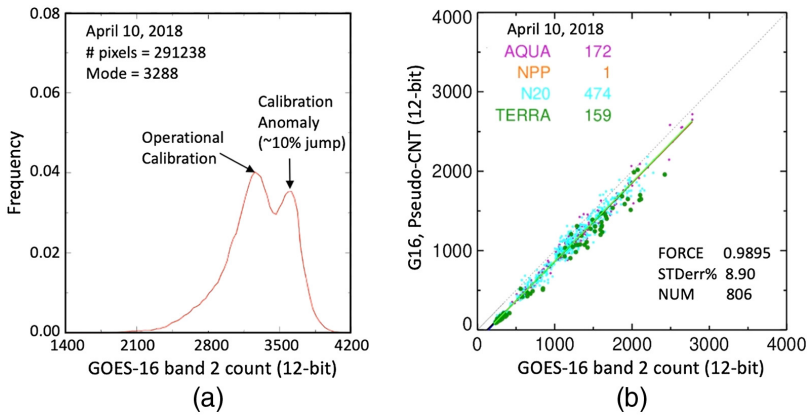

Fig. 10 (a) GOES-16 band-2 daily DCC PDF for April 10, 2018. (b) Daily ATO-RM GOES-16 count and imager pseudo-count pairs for the same day.

ATO-RM monthly gain behavior [Fig. 5(a)]. Remarkably, the ATO-RM and DCC-IT KFPDG were mostly within 0.5% over the record, and their 3-year gain difference was within 0.12%. The forward processing combined ATO-RM and DCC-IT daily monitoring algorithm approach was able to detect daily gain anomalies $> \pm 2.4\%$ of KFPDG, which is 3 times greater than the larger DCC-IT RMSE [Fig. 9(c)].

4 Conclusion

This study presented the ATO-RM and DCC-IT daily monitoring algorithms designed to detect near real-time GOES-16 imager L1B radiance anomalies. GEO imagers with onboard calibration systems introduce the possibility of incremental calibration updates and spurious short-term calibration events that need to be identified before retrieving GEO clouds and radiances as part of the CERES operational processing effort to avoid artifacts in the CERES flux record. The short-term nature of the calibration anomalies requires that the ATO-RM and DCC-IT algorithms be modified from their respective monthly algorithms by greatly expanding the number of daily ATO-RM pairs and DCC-IT identified pixels.

The daily ATO-RM algorithm increased the sampling by including GOES-16 with Terra-MODIS, Aqua-MODIS, NPP-VIIRS, and NOAA20-VIIRS ATO-RM pairs simultaneously, which were placed on the same radiometric scale using the inverse of their respective GOES-16 ATO-RM monthly gains as demonstrated in Eq. (2). The sampling was also enhanced by increasing the grid resolution as well as pairing multiple GOES-16 FD scans with the same imager overpass. Factors including the grid resolution, time difference, spatial homogeneity threshold, angle matching thresholds, and outlier filters decreased the daily linear regression standard error. However, only the angle matching thresholds and outlier filters also reduced the DTSE. Due to the limiting nature of the GOES-16 and imager angular matching, the angle matching thresholds need to be balanced with sufficient daily sampling. The resulting optimized angular threshold ATO-RM daily gains provided a DTSE of 0.75% over the 3-year record.

The combined monthly imager and GOES-16 ATO-RM pairs provided the lowest MTSE when compared with the individual imager MTSEs. The combined imager and GOES-16 ATO-RM pairs also predicted more accurately the on-orbit GOES-16 space CNT than those based on the individual imagers.

Similarly, the DCC-IT monthly algorithm was revised in order to capture over 100k daily DCC pixels. Revisions include increasing the (1) BT threshold, (2) GEO spatial domain, and (3) number of GOES-16 FD scans during the day. It was found that the DCC reflectance varies regionally, seasonally, and diurnally. The DCC reflectance was normalized accordingly, which removed a small seasonal oscillation in the DCC-IT daily monitoring gains. The GOES-16 DCC-IT daily monitoring algorithm produced a DTSE of 0.90% over the GOES-16 record.

A forward processing strategy is presented. For this GOES-16 band-2 study, any ATO-RM or DCC-IT daily gain that exceeds $\pm$3xRMSE or 2.4%, which is based on the previous daily gain differences, from the KFPDG is considered a possible calibration event anomaly. Both ATO-RM and DCC-IT daily monitoring algorithms identified Table 1 calibration events. Both ATO-RM and DCC-IT daily gains also introduced a few false positive calibration events. By requiring that both ATO-RM and DCC-IT daily gains identify the same calibration event, all false positives were successfully eliminated. Future GOES-16 L1B calibration anomalies that exceed $\pm$2.4% of the KFDPG can be cross-checked with the NOAA GOES-16 calibration event log web pages, if updated in near real time. Remarkably, the ATO-RM and DCC-IT daily gains were mostly within 0.5%. The ATO-RM and DCC-IT daily monitoring algorithms can easily be adapted to other GEO imagers as well as other visible channels.

Acknowledgments

This work was supported by the National Aeronautics and Space Administration Earth Science Enterprise Office through the CERES Project. The MODIS and VIIRS data were obtained from the NASA Langley Atmospheric Science Data Center Distributed Active Archive Center.

References

1. B. A. Wielicki et al., "Clouds and the Earth's Radiant Energy System (CERES): an earth observing system experiment," *Bull. Am. Meteorol. Soc.* **77**(5), 853–868 (1996).
2. N. G. Loeb et al., "Clouds and the Earth's Radiant Energy System (CERES) energy balanced and filled (EBAF) top-of-atmosphere (TOA) edition-4.0 data product," *J. Clim.* **31**(2), 895–918 (2018).
3. W. Su et al., "Next-generation angular distribution models for top-of-atmosphere radiative flux calculation from CERES instruments: validation," *Atmos. Meas. Tech.* **8**, 3297 (2015).
4. Q. Z. Trepte et al., "Global cloud detection for CERES edition 4 using terra and aqua MODIS data," *IEEE Trans. Geosci. Remote Sens.* **57**, 9410 (2019).
5. P. Minnis et al., "CERES MODIS cloud product retrievals for edition 4. Part I: algorithm changes," *IEEE Trans. Geosci. Remote Sens.* **59**(4), 2744–2780 (2021).
6. C. R. Yost et al., "CERES MODIS cloud product retrievals for edition 4. Part II: comparisons to CloudSat and CALIPSO," *IEEE Trans. Geosci. Remote Sens.* **59**(5), 3695–3724 (2021).
7. D. R. Doelling et al., "Geostationary enhanced temporal interpolation for CERES flux products," *J. Atmos. Ocean. Technol.* **30**(6), 1072–1090 (2013).
8. D. Doelling et al., "Geostationary visible imager calibration for the CERES SYN1deg edition 4 product," *Remote Sens.* **10**(2), 288 (2018).
9. K. Bassho et al., "An introduction to Himawari-8/9—Japan's new-generation geostationary meteorological satellites," *J. Meteorolog. Soc. Jpn.* **94**(2), 151–183 (2016).
10. T. J. Schmit et al., "A closer look at the ABI on the GOES-R series," *Bull. Am. Meteor. Soc.* **98**, 681–698 (2017).
11. T. J. Schmit et al., "Introducing the next-generation advanced baseline imager on GOES-R," *Bull. Amer. Meteor. Soc.* **86**, 1079–1096 (2005).
12. A. K. Inamdar and K. R. Knapp, "Intercomparison of independent calibration techniques applied to the visible channel of the ISCCP B1 data," *J. Atmos. Oceanic Technol.* **32**, 1225–1240 (2015).
13. https://www.star.nesdis.noaa.gov/GOESCal/goes_SatelliteAnomalies.php.
14. D. Hansen et al., "An overview of the GOES-R ground segment architecture," *Proc. SPIE* **7813**, 781304 (2010).
15. M. A. Lazzara et al., "The Man Computer Interactive Data Access System: 25 years of interactive processing," *Bull. Am. Meteorol. Soc.* **80**, 271–284 (1999).
16. M. Goldberg et al., "The Global Space-Based Inter-Calibration System (GSICS)," *Bull. Am. Meteorol. Soc.* **92**(4), 467–475 (2011).
17. https://www.data.jma.go.jp/mscweb/en/operation/calibration_portal.html.
18. https://www.eumetsat.int/website/home/Data/Products/Calibration/Instrumentstatusandcalibration/index.html.
19. https://www.goes-r.gov/spacesegment/abi.html.
20. D. R. Doelling et al., "Improvements to the geostationary visible imager ray-matching calibration algorithm for CERES edition 4," *J. Atmos. Oceanic Technol.* **33**, 2679–2698 (2016).
21. B. R. Scarino et al., "An online interface for calculating spectral band adjustment factors derived from SCIAMACHY hyper-spectral data," *IEEE Trans. Geosci. Remote Sens.* **54**(5), 2529–2542 (2016).
22. H. Bovensmann et al., "SCIAMACHY: mission objectives and measurement modes," *J. Atmos. Sci.* **56**(2), 127–150 (1999).
23. https://satcorps.larc.nasa.gov/cgi-bin/site/showdoc?mnemonic=SBAF.
24. A. Ignatov et al., "The usefulness of in-flight measurements of space count to improve calibration of the AVHRR solar reflectance bands," *J. Atmos. Ocean. Technol.* **22**, 180–200 (2005).
25. https://cloudsway2.larc.nasa.gov/cgi-bin/site/showdoc?mnemonic=CALIB-ED4.
26. https://satcorps.larc.nasa.gov/cgi-bin/site/showdoc?mnemonic=CALIB-UPRT.
27. D. R. Doelling et al., "An automated algorithm to detect MODIS, VIIRS and GEO sensor L1B radiance anomalies," *Proc. SPIE* **11151**, 111511T (2019).

28. R. Bhatt et al., "Clouds and the Earth's Radiant Energy System strategy for intercalibrating the new generation geostationary visible imagers," *J. Appl. Remote Sens.* **14**(3), 032410 (2020).
29. R. Bhatt et al., "Advances in utilizing tropical deep convective clouds as a stable target for on-orbit calibration of satellite imager reflective solar bands," *Proc. SPIE* **11127**, 111271H (2019).
30. Y. Hu et al., "Application of deep convective cloud albedo observation to satellite-based study of the terrestrial atmosphere: monitoring the stability of spaceborne measurements and assessing absorption anomaly," *IEEE Trans. Geosci. Remote Sens.* **42**(11), 2594–2599 (2004).
31. Q. Mu et al., "Optimization of a deep convective cloud technique in evaluating the long-term radiometric stability of MODIS reflective solar bands," *Remote Sens.* **9**, 535 (2017).
32. B. A. Wielicki et al., "Climate quality broadband and narrowband solar reflected radiance calibration between sensors in orbit," in *Proc. IEEE Int. Geosci. and Remote Sens. Symp.*, Boston, MA (2008).
33. F. Yu and X. Wu, "Radiometric inter-calibration between Himawari-8 AHI and S-NPP VIIRS for the solar reflective bands," *Remote Sens.* **8**, 165 (2016).
34. G. Hong et al., "Interannual to diurnal variations in tropical and subtropical deep convective clouds and convective overshooting from seven years of AMSU-B measurements," *J. Clim.* **21**(17), 4168–4189 (2008).
35. B. Tian, B. J. Soden, and X. Wu, "Diurnal cycle of convection, clouds, and water vapor in the tropical upper troposphere: satellites versus a general circulation model," *J. Geophys. Res.* **109**, D10101 (2004).
36. D. R. Doelling et al., "The characterization of deep convective clouds as an invariant calibration target and as a visible calibration technique," *IEEE Trans. Geosci. Remote Sens.* **51**(3), 1147–1159 (2013).
37. Y. Lee, M.-H. Ahn, and M. Kang, "The new potential of deep convective clouds as a calibration target for a geostationary UV/VIS hyperspectral spectrometer," *Remote Sens.* **12**, 446 (2020).

David R. Doelling leads the Clouds and the Earth's Radiant Energy System (CERES) Time Interpolated and Spatially Averaged Working Group and is responsible to temporally average the CERES fluxes and clouds into level-3 products. He incorporates hourly geostationary (GEO) derived broadband fluxes to infer the regional diurnal cycle requiring his focus on GEO imager calibration. He is the Global Space-based Inter-Calibration System visible calibration lead.

Conor Haney received his BS and MS degrees in atmospheric sciences from the University of Illinois at Urbana–Champaign, Champaign, Illinois, USA, in 2010 and 2013, respectively. He is currently a research scientist at the SSAI, Hampton, Virginia, USA, supporting NASA Langley Research Center contracts. He is responsible for maintaining the real-time visible sensor calibration of geostationary satellite imagers for the CERES project.

Rajendra Bhatt is currently supporting the CLARREO Pathfinder (CPF) project at NASA Langley Research Center as the deputy project scientist for intercalibration studies. Prior to joining CPF, he worked on the CERES project for 12 years developing techniques for in-flight calibration of geostationary and low-Earth-orbiting satellite imagers to assess their radiometric performance on orbit and ensure the usability of the satellite observations for climate studies.

Benjamin Scarino is employed by SSAI as a senior research scientist supporting the Climate Science Branch of the NASA Langley Research Center Science Directorate. As part of his work for the CERES program, he supports the development of global multispectral cloud and surface property retrieval algorithms as well as satellite calibration/validation efforts. He is a specialist on intercalibration techniques as well as on determining corrections for instrument spectral band differences.

Arun Gopalan received his BS degree in mechanical engineering from the University of Bombay, Mumbai, India, in 1991 and his MS degree in mechanical engineering from the State University of New York, Stony Brook, New York, USA, in 1993. He is currently a senior research scientist at the SSAI, Hampton, Virginia, USA, in support of the NASA Langley Research Center's CERES and Climate Absolute Radiance and Refractivity Observatory projects.